JGR Atmospheres

RESEARCH ARTICLE
10.1029/2024JD042771

Special Collection:
Chemistry and Climate Impacts of the Asian Summer Monsoon

An Integrated Analysis of Ozone and Carbon Monoxide Over the Western Pacific Using Satellite and Aircraft Measurements During the ACCLIP Summer Campaign 2022

Juseon Bak[1], Joowan Kim[2], Ja-Ho Koo[3], Laura L. Pan[4], Ju-Mee Ryoo[5,6], Paul A. Newman[7], Alessandro Franchin[4], Xiong Liu[8], Gonzalo G. Abad[8], Hyo-Jung Lee[1,9], WonBae Jeon[1,9], and Cheol-Hee Kim[1,9]

[1]Institute of Environmental Studies, Pusan National University, Busan, South Korea, [2]Department of Atmospheric Sciences, Kongju National University, Kongju, South Korea, [3]Department of Atmospheric Sciences, Yonsei University, Seoul, Republic of Korea, [4]Atmospheric Chemistry Observations and Modeling Laboratory, National Center for Atmospheric Research, Boulder, CO, USA, [5]Earth Science Division, Atmospheric Science Branch, NASA Ames Research Center, Moffett Field, CA, USA, [6]Bay Area Environmental Research Institute, Moffett Field, CA, USA, [7]NASA Goddard Space Flight Center, Code 610, Greenbelt, MD, USA, [8]Atomic and Molecular Physics Division, Smithsonian Astrophysical Observatory (SAO), Center for Astrophysics | Harvard & Smithsonian, Cambridge, MA, USA, [9]Department of Atmospheric Sciences, Pusan National University, Busan, South Korea

Key Points:

- The western Pacific region exhibited a complex interplay of monsoonal dynamics and transport in summer 2022 during the Asian Summer Monsoon Chemical & Climate Impact Project campaign
- Chemical tracers in the upper troposphere–lower stratosphere region reflected transboundary transport, convection, anticyclonic flow, and stratospheric intrusion
- TROPOspheric Monitoring Instrument's high spatial resolution improves daily identification of chemical tracer patterns over conventional satellite observations

Correspondence to:
C.-H. Kim,
chkim2@pusan.ac.kr

Citation:
Bak, J., Kim, J., Koo, J.-H., Pan, L. L., Ryoo, J.-M., Newman, P. A., et al. (2025). An integrated analysis of ozone and carbon monoxide over the western Pacific using satellite and aircraft measurements during the ACCLIP summer campaign 2022. *Journal of Geophysical Research: Atmospheres*, *130*, e2024JD042771. https://doi.org/10.1029/2024JD042771

Received 26 OCT 2024
Accepted 30 MAY 2025

Abstract The western Pacific exhibited a complex interplay of monsoonal dynamics and transport during the Asian Summer Monsoon Chemical & Climate Impact Project (ACCLIP) airborne field campaign in summer 2022. We analyze in situ observations of ozone (O_3) and carbon monoxide (CO) from 29 research flights—profiling over South Korea and cruising over the western Pacific —and balloon soundings in South Korea and Taiwan. In the upper troposphere (UT), a twofold enhancement in CO was observed across the mid-latitudes of the western Pacific, driven by large-scale uplift and outflow associated with the Asian Summer Monsoon (ASM) system. Observational evidence of enhanced UT O_3 in conjunction with its primary precursor, nitrogen dioxide (NO_2), was also presented. Satellite observations from the TROPOspheric Monitoring Instrument (TROPOMI) and Microwave Limb Sounder (MLS) were integrated with two selected flight cases to explore transport events and to provide broader spatial context. On July 31, the ASM anticyclone manifested in two distinct modes, South Asia High (SAH) and Western Pacific High (WPH). The SAH was filled with polluted air masses uplifted from the Asian boundary layer while the WPH was sustained by deep maritime convection. Both flight and satellite data captured polluted air parcels over the tropical western Pacific that had detached from the "main" anticyclonic eddy. By examining the case on August 6, we observed that the western Pacific was strongly modulated by low-level westerlies and the eastward extension of the ASM anticyclone and isentropic mixing near the tropopause.

Plain Language Summary Asia is home to 60% of the world's population and is the largest source of air pollution and greenhouse gases. Asian plumes affect air quality locally and have broader impacts on climate and weather patterns around the world through large-scale transport pathways. The Asian Summer Monsoon Chemical & Climate Impact Project (ACCLIP) airborne field campaign was carried out to collect atmospheric in situ measurements over the western Pacific in summer 2022, focusing on air masses transported from the Asian continent. This paper presents an observational analysis of aircraft in situ measurements of ozone and carbon monoxide along with satellite measurements during the ACCLIP campaign. The analysis addressed chemical signatures influenced by a complex interplay of atmospheric circulations. The potential for using aircraft measurements and high-resolution satellite data to complement each other in exploring the linkages between atmospheric composition and dynamics is demonstrated.

1. Introduction

Asia is home to 60% of the world's population and is the leading emitter of air pollutants and greenhouse gases due to rapid industrialization, urbanization, transportation activities, and land use changes across the region (Ramanathan & Feng, 2009; Vadrevu et al., 2017). Emissions in Asia surpass those on other continents and display an increasing trend (Amann et al., 2013; Kurokawa & Ohara, 2020; van Aardenne et al., 1999). China, in particular,

has become the primary emitter, with the release of most pollutant species peaking by 2015, while India's emissions have continued to rise, increasing its relative contribution to overall Asian emissions (Kurokawa & Ohara, 2020). These emissions impact local air quality and regional to global climates through atmospheric circulation (Bian et al., 2020; Jacob et al., 1999; Randel et al., 2010).

The Asian summer monsoon (ASM) anticyclone dominates the summer circulation in the upper troposphere–lower stratosphere (UTLS), spanning much of Asia and northern Africa (Hoskins & Rodwell, 1995) and comprising two major subsystems: The South Asian summer monsoon (SASM) and the East Asian summer monsoon (EASM) (Pan et al., 2024). It provides the key pathway through which convectively uplifted Asian boundary layer air can enter into the global stratosphere (von Hobe et al., 2021; Honomichl & Pan, 2020; Pan et al., 2016). Observational and modeling studies have found that the ASM anticyclone contains relatively high concentrations of tropospheric tracers—such as carbon monoxide (CO), methane (CH_4), and nitric oxide (NO)—compared with the surrounding regions, along with lower concentrations of stratospheric tracers (ozone (O_3) and nitrous oxide (N_2O)) in the UTLS region (von Hobe et al., 2021; Luo et al., 2018; Park et al., 2004). Furthermore, the ASM plays a critical role in modulating transboundary transport, net photochemical production, and deposition processes (Bak et al., 2022; He et al., 2008; Liu et al., 2023; Lu et al., 2018; Shen et al., 2022). For example, Bak et al. (2022) reported a bimodal seasonality of O_3 in the lower troposphere, with a minimum in late summer attributed to the transport of clean maritime air into the Korean Peninsula. In addition, Shen et al. (2022) demonstrated that monsoon-driven circulation significantly influences the source-receptor relationships of O_3 pollution over central and eastern China.

The redistribution of ozone and its precursors during summer is of importance due to the enhanced photochemical activity, which can lead to extremely high ozone episodes and elevate background concentrations in the free troposphere. The Asian Summer Monsoon Chemical & Climate Impact Project (ACCLIP) airborne field campaign was conducted in summer 2022 to investigate the impact of the ASM on UTLS chemical and aerosol composition over the western Pacific (Liang et al., 2025; Pan et al., 2024; Zhu et al., 2024). Funded by the National Aeronautics and Space Administration (NASA) and the National Science Foundation's National Center for Atmospheric Research (NCAR), the campaign consisted of 29 research flights from 31 July to 1 September 2022, using two aircraft: NASA WB-57 and NCAR Gulfstream V (GV). These flight observations have been providing new insights into stratospheric ozone chemistry. Specifically, Pan et al. (2024) discovered that the EASM convection plays a more prominent role in transporting chlorinated short-lived ozone-depleting substances (VSLSs) to the stratosphere than previously observed in the tropics. Building on this, Liang et al. (2025) further utilized in situ measurements of dichloromethane and chloroform from the WB-57 to estimate their contribution to stratospheric chlorine (~3.3%) and ozone depletion (~1 DU).

In this paper, we present an observational study of aircraft in situ measurements of O_3 and CO collected during the ACCLIP campaign. The focus is on the transport processes influencing the observed trace gas signatures, including ASM-driven transport in the UTLS region, mixing within the UTLS, and meteorologically driven transport in the lower troposphere. The vertical structures of O_3 and CO were characterized using ascent and descent flight profiles in the vicinity of the Korean Peninsula. The horizontal extent of high-altitude transport over the western Pacific was investigated using flight measurements made while cruising. To supplement the analysis of the spatiotemporal variability of O_3 profiles, ozonesonde soundings launched from three stations in South Korea and Taiwan in August 2022, as part of the ACCLIP campaign, were also used. Individual flight events were further analyzed using tracer-tracer and tracer-potential temperature correlations to address the underlying transport processes. In particular, we present a detailed analysis of two selected flights, complemented by satellite measurements and meteorological reanalysis data. The TROPOspheric Monitoring Instrument (TROPOMI) CO columns and Microwave Limb Sounder (MLS) CO mixing ratios were used to identify Asian pollution outflows in the transboundary layer and the UTLS region, respectively. In addition, TROPOMI O_3 profiles were used to explore ozone distributions in both the lower and upper troposphere. MLS measurements have been widely used to characterize the behavior of trace gases such as CO, H_2O, and O_3 within the ASM anticyclone, revealing the influence of deep convection and large-scale circulation on UTLS composition (e.g., Park et al., 2007; Randel et al., 2010; Vogel et al., 2015). As the MLS mission nears its end, this study highlights the potential of TROPOMI ozone profiles as a successor for investigating UTLS chemical structures, offering additional value through their unprecedented spatial resolution.

Table 1
List of Observational Data Sets From Airborne, Ozonesonde, and Satellite Measurements, Along With Meteorological Reanalysis

Data source[a]	Data type	DOI (revision or version number)	References
UASO3 (WB-57)	O_3 in situ	https://data.eol.ucar.edu/dataset/620.020 (R0)	Gao et al. (2012)
COMA (WB-57)	CO in situ	https://data.eol.ucar.edu/dataset/620.016 (R2)	Yates et al. (2025)
Fast O_3 (GV)	O_3 in situ	https://doi.org/10.26023/4JVW-8N8B-WQ0Q (R1)	Chiu et al. (2024)
Chemiluminescence (GV)	NO_2 in situ	https://doi.org/10.26023/4JVW-8N8B-WQ0Q (R1)	Ridley and Grahek (1990)
Aerodyne (GV)	CO in situ	https://doi.org/10.26023/2F7P-XVDS-S60Y (R1)	McManus et al. (2010)
Ozonesonde (Balloon)	O_3 sounding	Stations: - Anmyeondo https://doi.org/10.26023/39Y4-9RAB-5A0K (V2) - Pohang https://doi.org/10.26023/12PY-NA9V-Z903 (V1) - Pengjia Islet https://doi.org/10.26023/GH72-H4H2-RN13 (V1)	Smit et al. (2007, 2024)
TROPOMI (S5P)	Partial column O_3	https://doi.org/10.5281/zenodo.13988537 (V1)	Bak et al. (2025)
TROPOMI (S5P)	CO Total column	https://doi.org/10.5270/S5P-bj3nry0 (V2)	Borsdorff et al. (2018, 2023)
MLS (Aura)	CO profile	https://doi.org/10.5067/AURA/MLS/DATA2506 (V5)	Livesey et al. (2008, 2022)
MERRA-2	Meteorological reanalysis	https://doi.org/10.5067/A7S6XP56VZWS (V5.12.4)	Gelaro et al. (2017)

[a]Instrument (Platform) used for observation data sets and the meteorological data set (Merra2).

This research paper is organized as follows. The data sources are described in Section 2. In Section 3, we present the results and a discussion. The paper is summarized and the major conclusions are presented in the final section.

2. Materials and Methods

The observational and model data sets used in this study are listed in Table 1. The data sources include in situ measurements from aircraft and balloon-borne platforms, and remote sensing data from spaceborne nadir and limb-viewing instruments. Meteorological fields are obtained from the MERRA-2 reanalysis data set.

2.1. In Situ Measurements From Aircraft and Ozonesondes

The ACCLIP field campaign was based out of the Osan Air base (37.5°N, 127.1°E) in South Korea. Airborne observations were conducted over the western Pacific, to sample convective outflows of south Asian pollution transported by eastward transport via the ASM anticyclone in the UTLS. Data were recorded continuously between aircraft take-off and landing, providing both the vertical distribution during the ascent/descent phase and the spatial distribution during the cruise phase. Figures 1a and 1b shows the flight routes of the NCAR GV and NASA WB-57 aircrafts during their deployment in South Korea, with the flight altitude and time shown in Figure 1c. The WB-57 carried out 15 flights at cruise altitudes of 13–18 km, which targeted the lower stratosphere. Fourteen research flights, officially labeled RF01–RF14, were conducted by the GV aircraft to sample the upper troposphere (12−14 km), with large spatial coverage. Details of the airborne payloads are provided at https://espo.nasa.gov/acclip/wb-57_payload for WB-57 and https://www2.acom.ucar.edu/acclip/gv-payload for GV.

In this study, we principally used the 10 s average measurements of the in situ trace gas mixing ratios. Ozone mixing ratios were measured using the fast O_3 chemiluminescence instrument onboard the GV and the Unmanned Aircraft System Ozone Photometer (UASO3) onboard the WB-57. According to the data PIs, the total uncertainty of both ozone measurements is approximately 5%. NO_2 measurements from the GV platform is also used to supplement the analysis of ozone. A total of five different instruments were employed for CO observations. For our analysis, we used CO measurements from Aerodyne laser gas analyzer onboard the GV and Carbon mOnoxide Measurement from Ames (COMA) onboard the WB-57. The data PI of COMA reported a total uncertainty of 4–5 ppb. We also note that both GV and WB-57 data sets include instantaneous measurements of meteorological variables as well as GEOS-FP weather analysis products interpolated along the flight paths.

In support of the ACCLIP campaign, electrochemical concentration cell (ECC) ozonesondes were launched for the in situ profiling of O_3 and temperature from the surface to ∼35 km, with a vertical resolution of 100–150 m, at

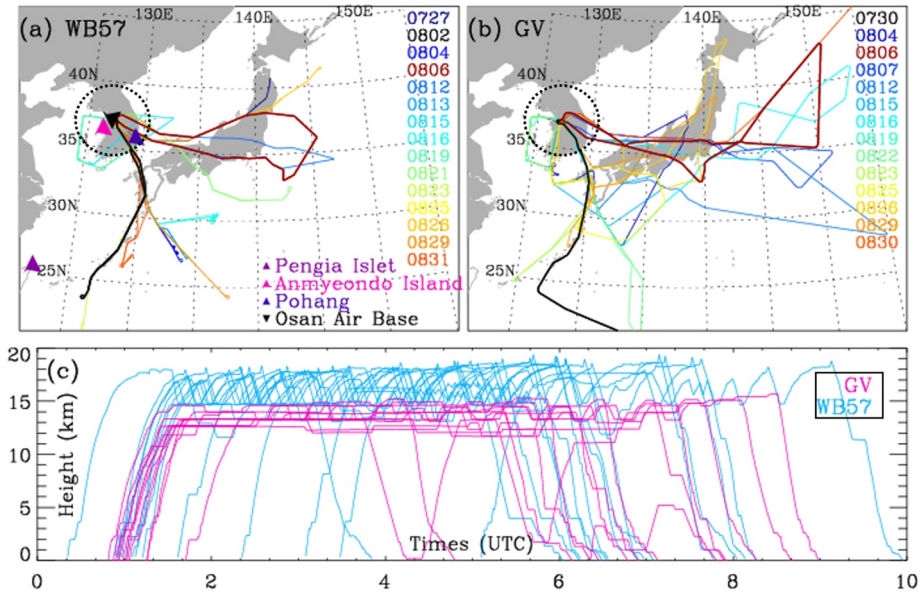

Figure 1. ACCLIP research flight tracks of the NCAR GV and NASA WB-57, projected in the spatial domain (a), (b) and flight height-observation time (UTC) domain (c). The 14 GV research flight (RF) paths are officially labeled RF01–RF14. Black and red-colored flights indicate the selected cases focused on Section 3.3. The black circle indicates a 300 km radius around Osan Air Base, South Korea (black triangle symbol). The three ozonesonde launch locations, as part of the ACCLIP campaign, are marked with colored triangle symbols.

the three stations marked with a triangle symbol in Figure 1a. The precision and accuracy of ECC sensors are better than ±3%–5 % and about ±5%–10%, respectively (Smit et al., 2007, 2024). In South Korea, ozonesondes have been regularly launched at Pohang station every Wednesday in the afternoon (13:30−15:30 local time (LT)) since 1995 by the Korea Meteorological Administration (KMA). For ACCLIP, KMA contributed four additional launches at the Pohang station in August 2022. In addition, a total of 38 ozonesondes were successfully launched from Anmyeon Island, South Korea, from 27 July to 2 September, mostly between 14:00 and 14:30 LT. These ozonesondes were operated by Kongju National University (KNU) and were funded by the National Institute of Environmental Research (NIER). A further eight ozonesondes were launched from Pengjia Islet, Taiwan (August 2022, 10:00−12:00 LT), by the Central Weather Administration (CWA) of Taiwan.

2.2. Satellite Measurements From the TROPOMI and MLS

We used satellite measurements from the TROPOMI, which is on board the Sentinel-5 Precursor (S5P) satellite launched in October 2017 (Veefkind et al., 2012), and the MLS, which is on board the Aura satellite launched in July 2014 (Waters et al., 2006). TROPOMI is a nadir-viewing, imaging spectrometer measuring radiances in eight spectral bands from UV to shortwave infrared (SWIR). With a wide swath of 2,600 km on the ground, TROPOMI achieves daily near-global coverage for multiple trace gases. The spatial resolution of TROPOMI is a few square kilometers (3.5×5 km^2 at nadir). The MLS instrument operates in a limb-viewing configuration, measuring the thermal microwave emission of the atmosphere along the sub-orbital track (5 km cross-track × 500 km along-track). Compared with nadir-viewing TROPOMI, MLS has lower spatial resolution and narrower cross-track coverage, but reliably resolves the vertical structures of trace gases with a vertical resolution of ∼3 km above 215 hPa.

In this study, O_3 profiles were retrieved from TROPOMI BUV measurements by adopting the OMI O_3 profile algorithm (Bak, Liu, et al., 2024). According to Bak et al. (2025), the retrieved O_3 profiles offer vertically resolved information up to ∼35 km, with peak sensitivity in the free troposphere and the lowermost stratosphere. CO measurements were taken from both the TROPOMI Level 2 CO total column product and the MLS/Aura Near-Real-Time L2 CO Mixing Ratio V005. TROPOMI clear sky observations provide CO total columns that are sensitive to the tropospheric boundary layer, retrieved in the 2.3 μm spectral range of the SWIR part of the solar

spectrum (Borsdorff et al., 2018, 2023), while MLS provides CO profiles with a high vertical resolution of 4–6 km in the recommended useful vertical range of 215–0.001 hPa (Livesey et al., 2008, 2022).

2.3. Meteorological Reanalysis

Meteorological parameters were obtained from the Modern-Era Retrospective Analysis for Research and Applications, version 2 (MERRA-2), which is available globally at 0.625° × 0.5° grids every 3 hr (Gelaro et al., 2017; GMAO, 2015). The available parameters include air temperature, geopotential height (GPH), and u- and v-wind components at 42 pressure levels from 1,000 to 0.1 hPa. The temperature profile was used to identify the thermal tropopause, which is defined as "the lowest level at which the temperature lapse rate decreases to 2 K/km or less" by the World Meteorological Organization (1957).

3. Results

3.1. Aircraft and Ozonesonde Profiles

We examine the vertical structures of O_3 and CO in the vicinity of the Korean Peninsula, using aircraft data collected during ascent and descent within a 300 km radius of the base camp, as shown in Figure 2. High-resolution flight measurements were averaged in 1 km altitude bins throughout August to assess the consistency between GV and WB-57 observations. This consistency is quantitatively supported by a correlation coefficient (R) of 0.7–0.9 for both gases. Notably, the GV and WB-57 profiles show close agreement in the lower troposphere during ascent, primarily due to their spatiotemporal coherence. The largest discrepancies occur above 5 km, where GV consistently measures higher concentrations of both O_3 and CO compared with WB-57.

Differences between ascent and descent profiles provide useful insight into the diurnal changes of chemical species and emission sources. The diurnal variation of O_3 was most pronounced near surface, where elevated concentrations were observed during afternoon flights. The surface O_3 levels increased from 50 ± 10 ppb in the morning ascents to as high as 90 ppb in the afternoon. In the free troposphere (2.5−13.5 km), O_3 mixing ratios gradually increased with altitude, ranging from 60 to 70–100 ppb. A sharp transition occurred within ±1 km of the mean thermal tropopause (∼15.41 km), where ozone values reached 120 ppb and exceeded 200 ppb within 1–2 km above the tropopause.

As expected, a strong enhancement in near-surface CO concentration was observed, reaching 290 ppb within 1-sigma of the mean value (200 ppb). This was followed by a local minimum of 70–80 ppb at an altitude of 4–5 km (Figures 2b and 2d). The significant variation in the near-surface CO concentration is attributed to the high sensitivity of ambient CO concentrations to local emission sources over the Korean Peninsula. In the upper free troposphere, CO exhibited a secondary peak at 12−13 km (110 ± 45 ppb), which was approximately 2 km below the thermal tropopause. This enhancement represents a key chemical signature of transport associated with the ASM anticyclone, as supported by modeling studies, satellite observations, and the StratoClim field campaign (von Hobe et al., 2021; Luo et al., 2018; Pan et al., 2016; Park et al., 2007). In the stratosphere (>∼15 km), CO gradually decreased from 80 ppb near the tropopause to 20−30 ppb at the upper limit of the flight altitude. This decrease in the CO concentration was in contrast to the rapid increase in O_3 concentrations over the same altitude range. The relatively uniform distribution of CO in the stratosphere suggests a state of chemical equilibrium.

Due to the high degree of consistency between the GV and WB-57 ascent profiles, the data sets were merged to explore the daily variation of O_3 over the Korean Peninsula. The combined profiles were then compared with ozonesonde soundings from launches at Anmyeondo Island, Pohang, and Pengjia Islet, as shown in Figure 3. These ozonesonde measurements effectively complement the limited spatiotemporal coverage of the aircraft profiles. The O_3 profiles exhibited clear vertical stratification and remained relatively stable near the tropopause throughout the campaign. Meteorological data (thermal tropopause and potential temperature) also indicated thermodynamic stability near the tropopause over the observation sites. In regions influenced by the inflow of clean marine boundary layer air, lower free-tropospheric O_3 concentrations are often higher than those in the boundary layer, particularly during summer (e.g., Bak et al., 2022). The lower free-tropospheric O_3 concentrations generally exceeded 60 ppb over the Korean Peninsula during the campaign, 20 ppb higher than those observed at Pengjia Islet. At Anmyeondo Island, daily ozonesonde soundings reveals high O_3 values (100−140 ppb) in the upper troposphere on 4−6 August and 16−17 August, despite the thermodynamic stability of the

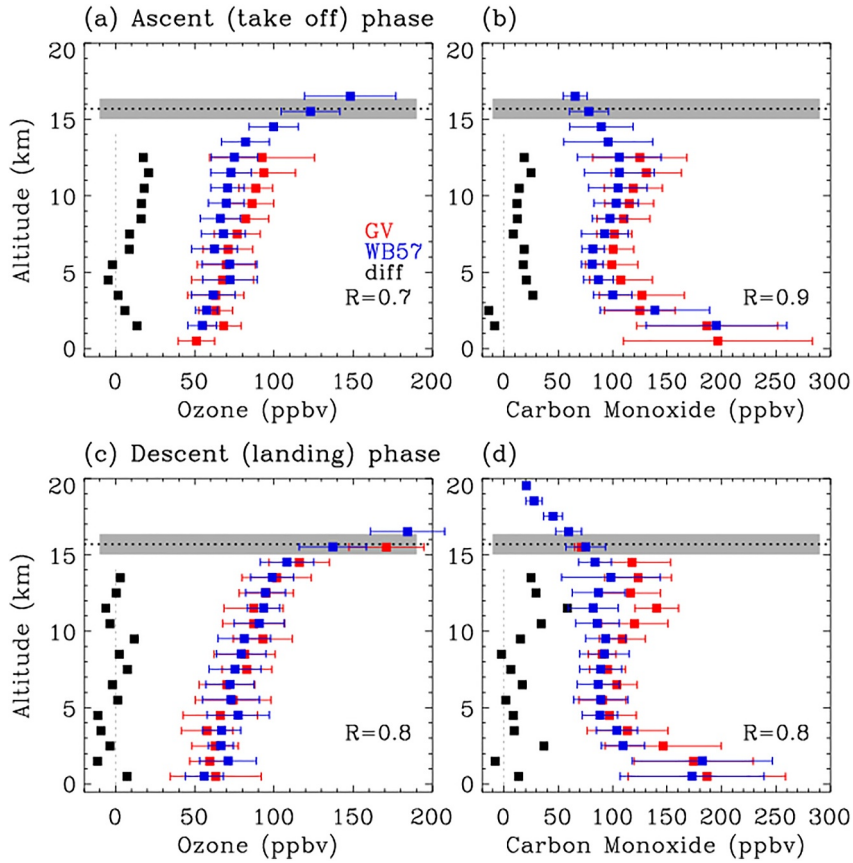

Figure 2. Vertical profiles of ozone (O_3) and carbon monoxide (CO) mixing ratios obtained from the GV (red) and WB-57 (blue) aircraft during their ascent (a), (b) and descent (c), (d) phases. The average differences between GV and WB-57 are plotted along with the correlation coefficient value in the legend. The data were restricted to the region within 300 km of base camp in South Korea, as delineated by the black circle in Figure 1a. The square symbols and error bars represent the mean and ±1 σ standard deviation for 1 km binned data. The tropopause height is 15.41 ± 1.42 km along the GV flight path, as interpolated from the GEOS-FP_MET (mean: dashed line, 1σ: shaded).

tropopause. Both aircraft and ozonesondes also showed abnormally low O_3 values throughout the troposphere during 30 July–2 August, suggesting the long-range transport of O_3-poor, marine-influenced air masses from the tropics toward the Korean Peninsula (Figure 3b). This observation is addressed in more detail in the following section.

3.2. Tracer Characteristics in the UTLS From Aircraft Measurements

The cruise data from all GV and WB-57 long-range flights were aggregated to examine the horizontal extent of the high-altitude transport processes over the western Pacific region, with the results shown in Figure 4. In the UT, there were enhancements in the CO concentration across the field domain, which originates from polluted Asian continental air masses transported by the ASM anticyclone (Figure 4c). Particularly high CO levels (>150 ppb) were observed in the latitude range of 30–40°N, where the Tibetan Plateau is situated. However, the corresponding response in O_3 abundance was relatively modest, even though CO is a key precursor of O_3 (Figures 4a and 4c). At altitudes above 15 km, there was still an inflow of polluted continental air with high CO levels (>100 ppb) near 130°E (Figure 4d). Elsewhere, CO abundance was strongly negatively correlated with that of O_3 due to the inflow of stratospheric air.

To explore the interplay between distinct air masses and the transition regions where mixing occurs, the spatial distributions of O_3 and CO shown in Figure 4 were projected into tracer–tracer space (Figure 5a), with each of 14 GV flight number color coded. The WB-57 observations were matched to the closest GV flight date and assigned colors accordingly. The observed tracers formed the well-known L-shaped relationship between

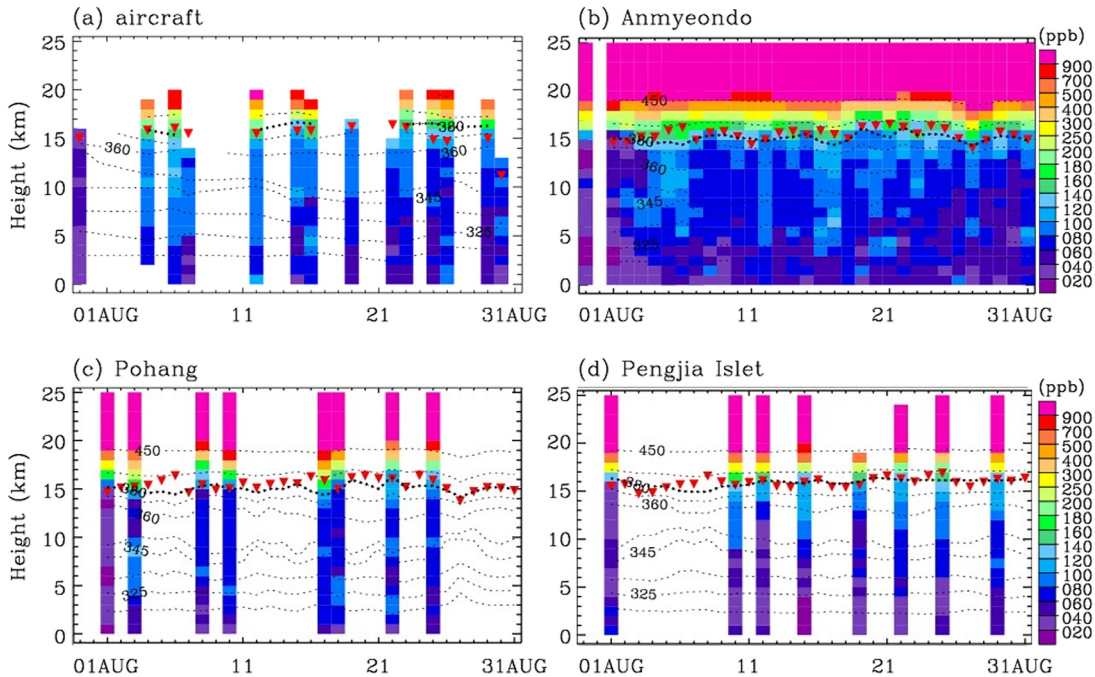

Figure 3. (a) Daily ozone profiles obtained from merged GV and WB-57 ascending measurements, shown alongside (b)–(d) ozonesonde profiles from three stations in South Korea and Taiwan. Overlaid potential temperature contours (dashed lines) and thermal tropopause heights (red symbols) are based on the GV flight path in panel (a), using the accompanying GEOS-FP_MET data. For panels (b)–(d), these meteorological variables are interpolated from daily MERRA-2 reanalysis data.

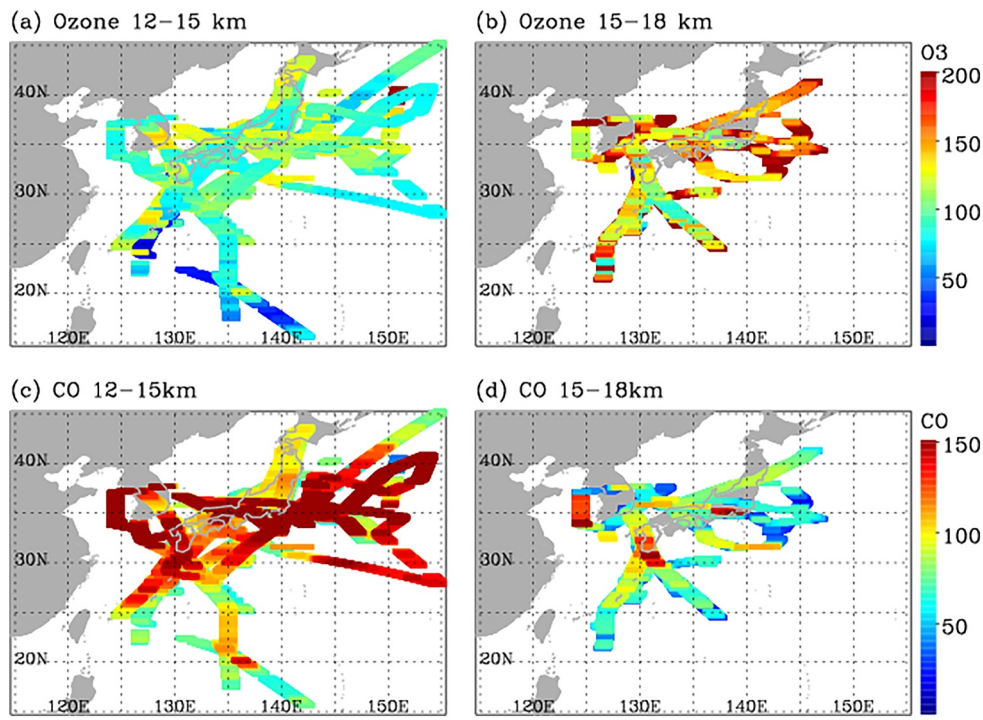

Figure 4. Horizontal maps of the O_3 and CO mixing ratios (ppbv) for all GV and WB-57 flights, produced by binning into non-overlapping grids through averaging at 1-min intervals for the upper troposphere (UT, 12−15 km) and lower stratosphere (LS, 15−18 km).

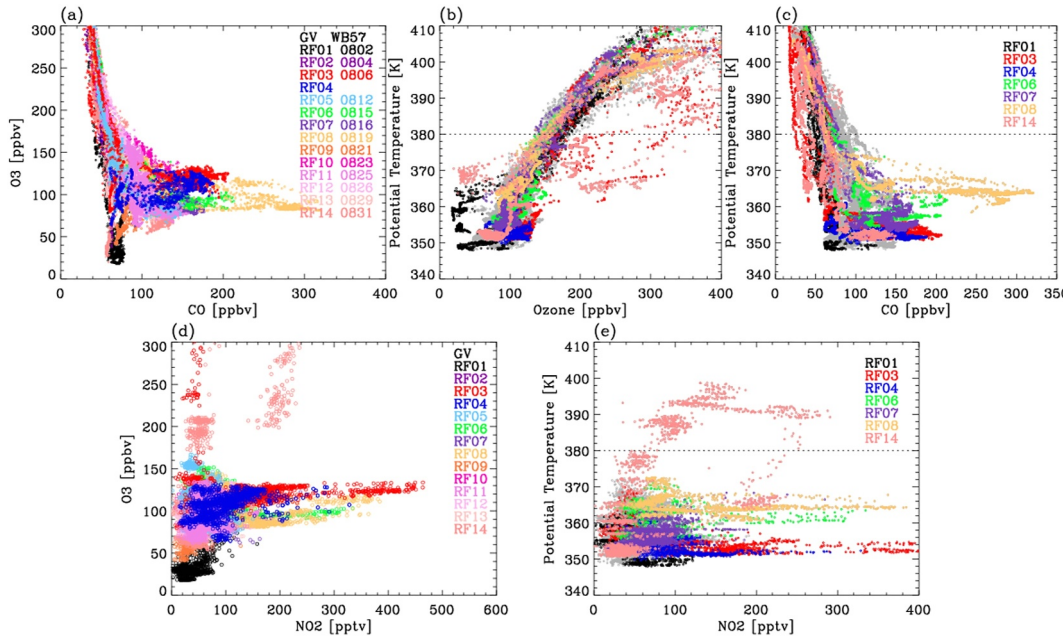

Figure 5. (a) Scatter plots of O_3 versus CO at cruise altitudes (12−18 km), with different colors representing the 14 GV research flights (RF01–RF14). WB-57 data are matched to 10 GV flight dates and three nearest dates, excluding RF04 to avoid duplication. The legend lists GV flights and their corresponding WB-57 dates. Mixing ratios are shown in potential temperature coordinates: O_3 (b) and CO (c). Anomalous tracer measurements are highlighted in colors while other measurements are shown in gray. The 380 K isentropic line (dotted) indicates the approximate location of the tropopause. Panels (d) and (e) show O_3 versus NO_2 and NO_2 versus potential temperature, respectively.

stratospheric and tropospheric tracers (Diao et al., 2015; Gettelman & Sobel, 2000; Pan et al., 2014, 2016, 2024; Vogel et al., 2011). The tropospheric branch (horizontal line of the "L" shape) is largely composed of GV observations from RF08 (August 19), which captured CO plumes ranging from 200 to 320 ppb. The vertical branch was thinner, reflecting the more uniform nature of the stratospheric air, with CO equilibrium (∼50 ppb) despite the sharped increase in the O_3 concentration. The corner where the horizontal and vertical branches meet can be interpreted as a transition zone, representing a mixture of air masses from both tropospheric and stratospheric origins. The depth and extent of this region reflected the day-to-day variability in mixing intensities and source influences. The outmost corner of the L-distribution, characterized by anomalously low O_3 and CO concentrations, likely represents cleaner marine air, which was consistently detected in ozonesonde profiles during late July and early August (Figure 3b).

Figures 5b and 5c show the vertical distribution of tracers in potential temperature (θ) coordinates (altitude = 12−18 km), with the isentropic line θ = 380 K indicated. According to Pan et al. (2024) and Smith et al. (2025), the thermal tropopause during the ACCLIP campaign extends from 360 to 380 K. Therefore, the 380 K surface marks the upper boundary of the tropopause transition layer. The O_3 profiles during RF03 and RF14 display a fragmented structure in the upper troposphere, with irregular spikes exceeding 150 ppb. These spikes suggest the transport of O_3-rich air masses from the stratosphere to the troposphere along isentropic surfaces. Concurrently, CO concentrations dropped to ∼40 ppb, further supporting the stratospheric origin of these air masses. In the free troposphere (θ < 370 K), abnormally high CO levels (>150 ppb) were observed during flights on 6, 7, 15, 16, and 19 August. The corresponding O_3 levels remained largely unperturbed, except during RF03 and RF04, when a 20-ppb increase was detected below the 360 K isentrope. As shown in Figure 5d, this O_3 enhancement coincided with elevated NO_2 levels exceeding 200 ppt, suggesting a possible contribution from photochemical production or the co-transport of precursors. This interpretation is further supported by Figure 5e, where NO_2 peaks align well with CO enhancements in Figure 5c, indicating that both species were likely transported together within the same polluted air masses (RF03, RF04, RF06, RF08).

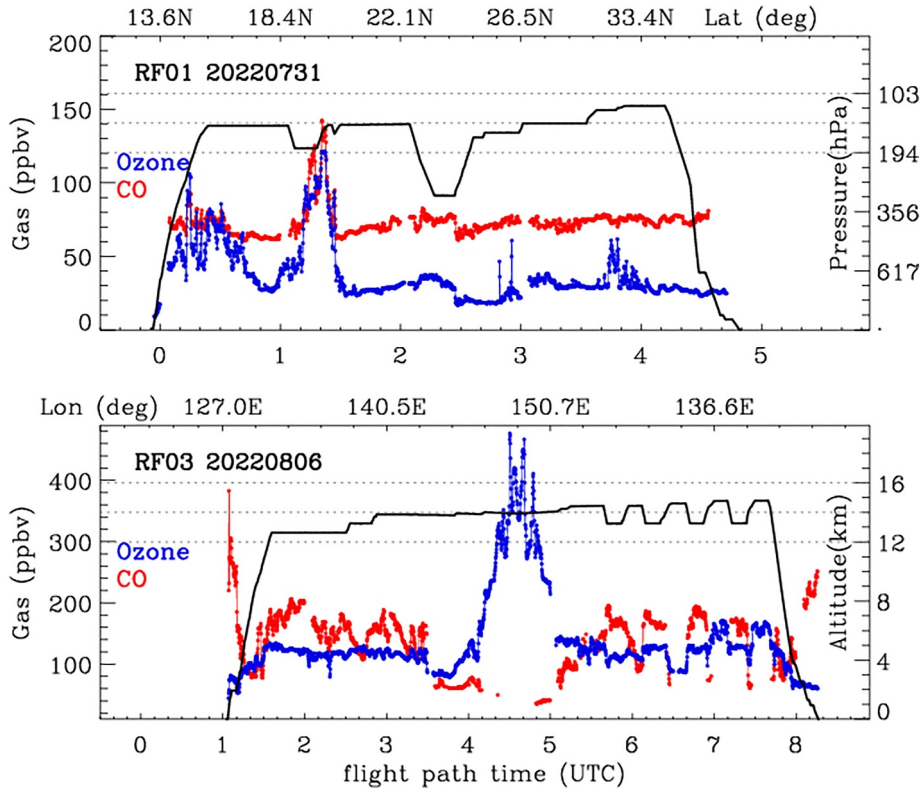

Figure 6. Mixing ratios of O_3 (blue) and CO (red) and the altitude (black) measured by the GV aircraft on 31 July (RF01) and 6 August 2022 (RF03), respectively. The mixing ratios are plotted as a function of the flight path time (UTC) in the lower *x*-axis and the latitude/longitude in the upper *x*-axis.

3.3. Satellite Observations on Two Flight Cases: 31 July and 6 August 2022

TROPOMI and MLS make nadir- and limb-viewing measurements, respectively. Each approach has its own set of unique advantages and limitations (e.g., in terms of spatial or temporal representativeness). Here, TROPOMI provides daily global observations of trace gas columns with a city-scale spatial resolution, while MLS measures high-vertical-resolution profiles of upper troposphere and stratosphere trace gases, but with insufficient samplings and global coverage on a monthly timescale. Therefore, a 5-day composite of MLS data is used to depict the CO map on 5° × 5° grids. The spatial distribution of O_3 is based on a single day of TROPOMI observations while CO columns were averaged over 3 days due to data gaps resulting from the rigorous cloud filtering. The satellite measurements were integrated to investigate the transport pathways affecting the anomalous tracers measured by the GV aircraft during the flights on 31 July (RF01) and 6 August (RF03), respectively. The RF01 departed from Broomfield, Colorado, USA, with measurements covering the transit segment from Guam to Osan. This flight encountered a narrow plume of elevated CO and O_3 concentrations around 1:20 UTC when flying over the tropical Pacific (Figure 6a). The RF03 exhibits a complex feature influenced by both polluted boundary layer air, which was CO-rich, and stratospheric air, which was O_3-rich (Figure 6b). The integrated results are presented separately for the lower troposphere (Section 3.3.1) and the upper troposphere (Section 3.3.2).

3.3.1. Analysis of the Lower Tropospheric Composition

Satellite measurements can supplement aircraft measurements in the ACCLIP campaign by accessing the spatiotemporal areas beyond the mission's reach, particularly in the lower troposphere. Figure 7 shows maps of tropospheric O_3 and total CO columns based on TROPOMI measurements for two selected dates, together with meteorological data at 850 hPa taken from MERRA-2 reanalysis results. The 950−400 hPa O_3 column was used for the analysis of summertime lower troposphere to avoid any stratospheric influence and increase the information content (Shen et al., 2019). The CO column concentrations are inherently most sensitive to CO

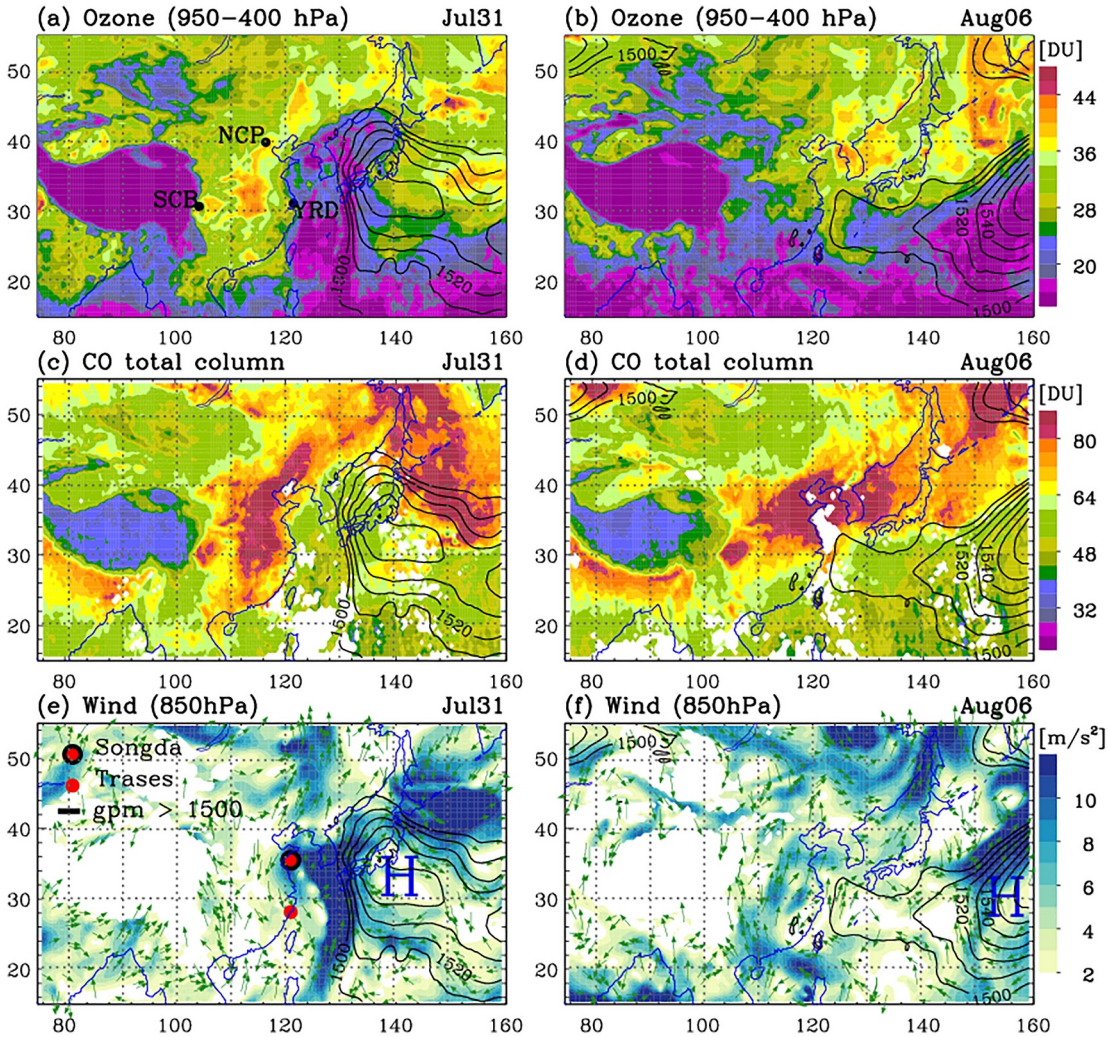

Figure 7. (a–b) Tropospheric 950−400 hPa O_3 column, and (c–d) total CO columns from TROPOMI observations on 31 July and 6 August 2022, with (e–f) MERRA-2 wind fields at 850 hPa where the wind speed exceeds 3 m/s^2. The contours of geopotential heights are overlaid to mark the high pressure system (black, minimum: 1,500 gpm, intervals: 10 gpm). Red circles mark the location of Typhoons Songda and Trases on July 31. NCP, YRD, and SCB refer to the North China Plain, Yangtze River Delta, and Sichuan Basin, respectively.

enhancement in the troposphere below 5 km due to the application of SWIR averaging kernels (Borsdorff et al., 2023), and TROPOMI CO measurements therefore represent the boundary layer information.

Horizontal wind speed and direction can suggest possible transport routes of chemical tracers. In particular, the Western Pacific Subtropical High (WPSH) plays a crucial role as a prevailing circulation system affecting summer weather and climate in East Asia (Guan et al., 2019). The WPSH is conventionally measured by the 5,880 gpm geopotential height (GPH) at 500 hPa (Zhou & Li, 2002) while the 1,490 gpm contour at 850 hPa has also been recognized as an indicator of the WPSH (S. Wang & Yuan, 2018; Zhao et al., 2022). As seen in Figure 7, the GPH contours (>1,500 gpm) effectively delineate the location of the WPSH and reveal its significant variation between the two case study dates.

In the case of July 31, Typhoons Songda and Trases were sequentially aligned over the southeastern sea off the Korean Peninsula (red circles in Figure 7e). Strong southerly winds developed between the cyclonic circulation to the east of the typhoons and the anticyclonic flow associated with the western flank of the WPSH. In this situation, maritime air masses were transported from the remote tropics toward the Korean Peninsula and Japan, along with heavy rainfall. The TROPOMI retrievals capture an elongated area of low O_3 and low CO in the region heavily influenced by the enhanced southerlies (Figures 7a and 7c). Additional details on the duration and vertical extent

of the southerly transport can be obtained from ozonesondes. As mentioned, abnormally low ozone levels of 25 ppb were consistently recorded through the troposphere in ozonesondes launched between July 30 and August 2 at stations in both Korea and Taiwan (Figure 3), suggesting the occurrence of rapid uplift reaching the tropopause. Meanwhile, hot spots of CO columns were broadly distributed across most of China and Indo-Gangetic Plain. O_3 columns were concentrated over the North China Plain (NCP), Yangtze River Delta (YRD), and Sichuan Basin (SCB).

As seen in Figure 7f, the weather pattern of August 6 illustrates that westerlies intensified over the Northeast Asia while southwesterlies and southeasterlies prevailed over southern China. This is likely associated with the southeastward shift of the WPSH system from its position in the earlier case on July 31 and its expansion to the East China Sea. As a result, O_3 and CO were redistributed regionally and intercontinentally. Compared with the earlier case, CO columns were significantly reduced in the southern China, which received oceanic air masses from the South China Sea and the Bay of Bengal. The central China regions exhibit that O_3 columns were significantly reduced, while CO columns, directly emitted from sources, were enhanced, indicating that the weather was unfavorable for ozone production. Notably, the redistribution of Asian pollutants toward the western Pacific is clearly evident in the spatial distribution of CO and O_3 being carried by intensified westerlies.

3.3.2. Analysis of the UTLS Composition

On a seasonal scale, the main body of the ASM anticyclone (ASMA) forms over the Tibetan Plateau (80°–95°E), referred to as the Tibetan anticyclone or the South Asian High (SAH). The intraseasonality of UTLS chemical composition is closely associated with changes in the location of ASMA centers. On a synoptic scale, eddy-shedding of the ASM anticyclone causes irreversible mixing in the surrounding air, altering its chemical composition. The western Pacific is often linked with the eastward eddy shedding region of the main (Tibetan) anticyclone (Honomichl & Pan, 2020; Pan et al., 2016; X. Wang et al., 2022). Honomichl and Pan (2020) suggested that eastward eddies breaking off from the ASM air mass can be transported to either the lower northern extratropical region or eastward along with the subtropical jet via the western Pacific mode of the large-scale ASMA. In preparation for the ACCLIP campaign, Pan et al. (2022) conducted a multimodel chemical investigation of ASM transport, highlighting the need for airborne in situ measurements to link the core region of the ASM with the western Pacific UTLS. The July 31 flight event of this 2022 ACCLIP field campaign can be connected with an eastward eddy-shedding event.

To supplement the in situ O_3 along the GV flight path, the TROPOMI partial ozone columns were converted into mixing ratios and interpolated at 150 hPa, corresponding to the GV cruise altitude. Figure 8 shows that ozone is strongly anticorrelated to GPH in the upper troposphere. On July 31, the UT anticyclone appeared with two cores of relatively high GPH values in Southeast Asia (88°E, 28°N) and the western Pacific (130°E, 32°N), respectively. Correspondingly, the "center-low and edges-high" pattern of TROPOMI O_3 ppb aligns with the "center-high and edges-low" pattern of GPHs. In contrast, the Southeast Asia High (SAH) was filled with CO-rich air while the Western Pacific High (WPH) was characterized by CO-poor air, as captured by MLS (Figures 9a–9c). In particular, the lowest concentrations of ozone (20–30 ppb) and CO (~70 ppb) were sampled when the GV flew over the WPH, which originated from the fresh, convective outflow of the typhoons, Songda and Trases. In Honomichl and Pan (2020), the three primary pathways affecting the WPH air masses were diagnosed using backward trajectories, including the ASM anticyclone circulation and the vertical updrafts from either the Asian boundary layer or the marine boundary layer. Interestingly, the GV flight intersected both the "clean" air lifted from the marine boundary layer of the western Pacific near the center of WPH and "polluted" air shaded from the ASM anticyclone near 20°N and 137°E. The dirty air contains high-O_3 (~120 ppb) and high-CO (150–200 ppb). The TROPOMI data also captures the eddies breaking off from the ASM air mass, which form an elongated filament of enhanced concentrations in the north-south direction at the eastern edges of the WPH. This eddy shedding transport is also evident in the MLS CO map, capturing the elongated filament of high CO at 215 hPa over the eastern edges of WPH (Figure 9a). In addition, the MLS CO at 147 hPa indicates the confines of the ASM processed air toward the western Pacific (Figure 9b), whereas at 100 hPa uplifted Asian boundary layer air was confined near the SAH center (Figure 9c).

On August 6, the ASM anticyclone emerged with a single center over the Tibetan plateau (Figure 8e). Compared with the earlier case, the SAH at 150 hPa extended northward and eastward with enhanced strength, creating a wide pool of O_3-poor and CO-rich air that spanned much of Southeast Asia (Figures 8b and 9d–9f). The MLS

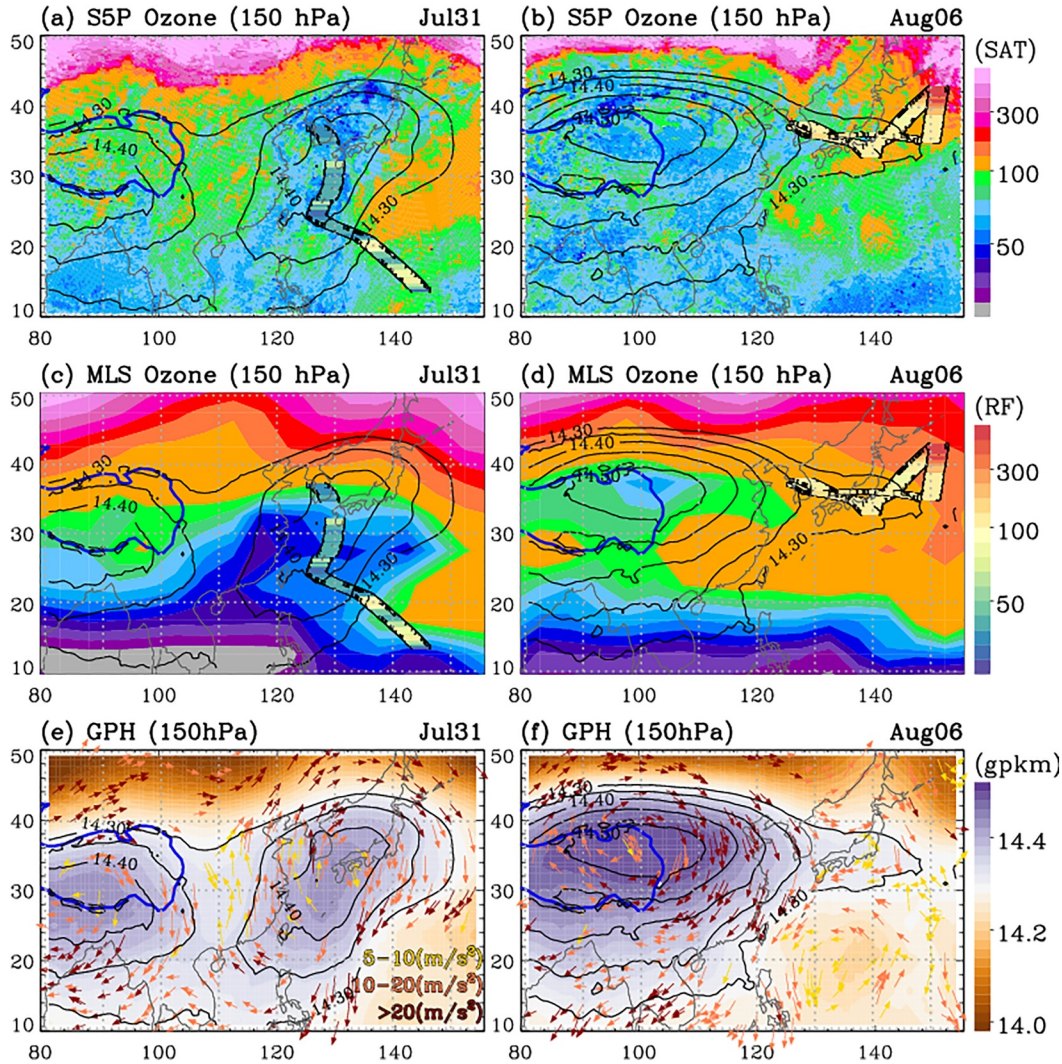

Figure 8. Upper-level distribution of ozone mixing ratios from (a–b) TROPOMI and (c–d) MLS, along with in situ O_3 mixing ratios along the GV flight track. (e–f) Wind speed (shaded) and wind direction (vector) at 150 hPa taken from MERRA-2. Geopotential height (GPH) contours are overlaid. The blue line represents the 3,000 m altitude of the Tibetan Plateau.

mixing ratios at 215 hPa suggest two hotspot regions of convective transport (CO > 120 ppb), centered over the southwestern flank of the Tibetan Plateau and the northern part of the Indian subcontinent. In addition, the stronger westerly jets on the northern edge of the ASMA, which act as a barrier to meridional transport, clearly separate the low-O_3 amount in the tropics from the higher concentrations in the extratropics, creating a strong O_3 gradient. Conversely, the meridional transport of high-O_3 air occurred over Japan, where the westerly jet was relatively weak and rotated southward, creating a mixture of tropospheric and stratospheric air. The GV aircraft flew both inside and outside the anticyclone. On the eastern edge of the anticyclone, it sampled CO-rich air with mixing ratios of 150–220 ppb at cruising altitudes below 13.5 km, whereas CO-poor air was collected just at higher altitudes. This suggests that the occurrence of the ASM transport toward the western Pacific was limited to specific altitudes. The coherently sampled ozone was found to be nearly invariant with a mixing ratio of ∼120 ppb. Moreover, the flight sampled stratospheric air with increasing O_3 exceeding 400 ppb at the lowest CO value between 3:30 and 5:00 UTC when crossing the westerly jet. As shown in Figure 8b, the TROPOMI measurements were found to have the capability to capture the transition between tropospheric and stratospheric O_3 observed by the GV aircraft. However, the MLS ozone data shown in Figures 8c and 8d exhibit significant discrepancies in resolving the fine structure near the edge of the anticyclone, presumably due to the limited spatiotemporal resolution of MLS observations and the day-to-day variability of ASM transport.

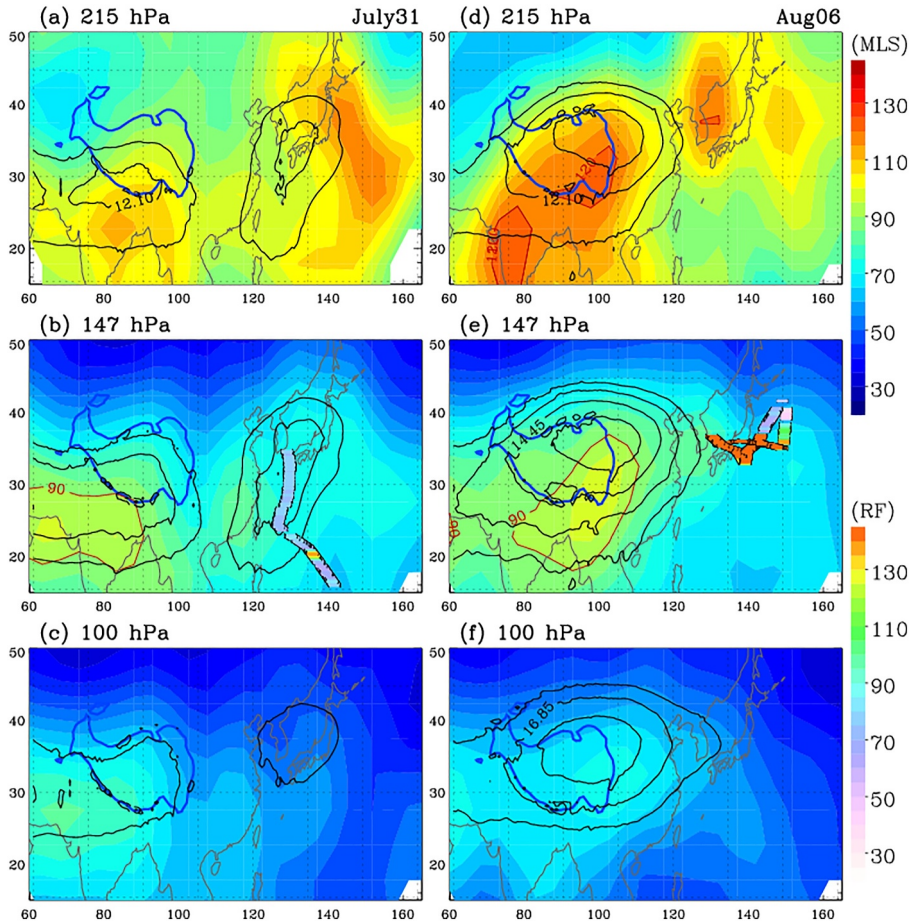

Figure 9. The MLS measured CO mixing ratios at 215, 147, and 100 hPa. Five days of MLS data centered on a given date were interpolated onto 5° × 5° longitude−latitude grids to map the horizontal distribution of CO. The GV in situ CO measurements are overlaid on the CO map at 147 hPa. The black contours of geopotential height indicate the existence of upper-level anticyclones. The blue line represents the 3,000 m altitude of the Tibetan Plateau.

4. Conclusions

In this study we examined in situ CO and O_3 measurements from 29 research flights and ozonesonde launches conducted during the ACCLIP campaign. O_3 soundings indicate the increasing mixing ratios from 50 ppb in the boundary layer to 70−90 ppb in the middle to upper troposphere, with the rapid enhancement near the tropopause (∼15 km). CO profiles reveal two peaks: one due to local emissions near the surface and the other due to the ASM plume in the upper troposphere (∼13 km). The high-altitude enhancement was evident across the western Pacific, particularly within the latitude range of 30–40°N encompassing the Tibetan Plateau. While no distinct O_3 enhancement was observed in direct response to the elevated carbon monoxide (CO) levels, a coherent increase in both CO and NO_2 was evident. Notably, the NO_2 enhancements were associated with elevated O_3 concentrations in the upper troposphere, with O_3 mixing ratios reaching 90–130 ppbv, possibly indicating the impact of monsoon-driven precursor transport on in situ photochemical ozone production. Among the 14 paired GV and WB-57 aircraft flights, five days were identified as Asian monsoon plume events (RF03, RF04, RF06, RF07, RF08), during which elevated CO concentrations (>150 ppb) were transported into the mid-latitudes of the western Pacific. In addition, isentropic transport was observed during RF03 and RF14, and convective transport occurred on RF01 and RF14. To further investigate transport pathways and their origins, we analyzed two case studies—31 July and 6 August—by integrating flight observations with satellite data, including high-spatial-resolution TROPOMI CO/O_3 columns and high-vertical-resolution MLS CO profiles. This study highlights the advantages of TROPOMI's high-spatial-resolution in capturing fine-scale trace gas variability associated with ASM eddies, stratosphere-troposphere exchange (STE), convectional transport, and transboundary transport. The

reliability of these observations is demonstrated through their consistency with findings from ACCLIP research flights. The characteristics of the two cases over East Asia and the western Pacific can be summarized as follows:

On 31 July, TROPOMI lower tropospheric columns indicated the intrusion of very low O_3 and CO abundances from the tropics through the Korea–Japan Sea. This transport was attributed to a narrow band of strong southerly winds that formed between the west of the WPSH and east of the typhoon pathway. The impact of rapid convective transport associated with typhoons was evident during this episode. Ozonesondes revealed a consistently abnormally low O_3 concentration of ~25 ppb through the troposphere up to the tropopause at both the Korean and Taiwan sites. The TROPOMI O_3 data also revealed a convectively lifted poor-O_3 air mass trapped within the upper-level WPH, which resulted in the formation of a large area with low O_3 concentrations. In particular, TROPOMI data provided a crucial insight into where the eastward eddies broke off from the ASM air mass. They showcased the elongated structure of elevated O_3 levels associated with the ASMA circulation, extending to the narrow plume of high O_3 (120 ppb) and CO (150 ppb) air observed in the GV flight data at low latitudes. The MLS CO data corroborated these findings, revealing strongly correlated transport signatures with low CO in the center of the WPA and high CO concentrations on its western edge.

On 6 August, satellite data identified transboundary pollution originating in China and spreading to the western Pacific, with elevated levels of O_3 and CO. This occurred under the prevailing westerlies while the WPSH was shifted southeastward. Compared with an earlier case, the strengthening and expansion of the ASM anticyclone led to the formation of extensive pools of O_3-poor air with high CO concentrations in the upper atmosphere. This extended across much of the Asian region and also impacted the western Pacific. The MLS CO data effectively identified the convective area in the South Asian region due to a high vertical sensitivity, while the high spatial resolution of the TROPOMI O_3 data captured transient mixing between the UTLS, in close agreement with findings from the GV research flights.

We explored the the transport signatures of the chemical tracers O_3 and CO, with a focus on distinct cases of the western Pacific during the ACCLIP summer 2022 campaign. Beyond the two case studies presented, integrating satellite data and other flight events can further contribute to understanding the transport pathways affecting atmospheric composition over the western Pacific and their implications for climate and radiative forcing. In the following studies, the satellite measurements will supplement aircraft measurements in the ACCLIP campaign by accessing the spatiotemporal areas beyond the mission's reach for the climatological analysis and the global analysis.

Conflict of Interest

The authors declare no conflicts of interest relevant to this study.

Data Availability Statement

The NASA WB-57 and NCAR GV aircraft data used in this study are available from the NASA Langley Research Center Atmospheric Science Data Center (NASA, 2025) and the NSF NCAR EOL data archive (Honomichl, 2023), respectively. Ozonesonde data were obtained for three locations: Anmyeon (Kim & Koo, 2024), Pohang (Shin et al., 2023), and Pengjia (Chen & Chou, 2022). Satellite data include MLS CO profiles (Schwartz et al., 2020), TROPOMI CO column data (Copernicus Sentinel data processed by ESA et al., 2019), and TROPOMI ozone profile data (Bak, Liu, & Gonzalez Abad, 2024). The MERRA-2 reanalysis data (inst3_3d_asm_Np) were obtained from the NASA Earthdata website (GMAO, 2015).

Acknowledgments
We thank the NASA, NCAR, KMA, CWA, and Copernicus for providing their measurements and analysis data. We especially acknowledge the ACCLIP instrument PIs for ozone, CO, and NO_2. This research has been supported by the Basic Science Research Program through the National Research Foundation of Korea (NRF) funded by the Ministry of Education (Grants RS-2020-NR049592 and RS-2021-NR058144).

References

Amann, M., Klimont, Z., & Wagner, F. (2013). Regional and global emissions of air pollutants: Recent trends and future scenarios. *Annual Review of Environment and Resources*, *38*(1), 31–55. https://doi.org/10.1146/annurev-environ-052912-173303

Bak, J., Liu, X., Abad, G. G., & Yang, K. (2025). An extension of ozone profile retrievals from TROPOMI based on the SAO2024 algorithm. *Remote Sensing*, *17*(5), 779. https://doi.org/10.3390/rs17050779

Bak, J., Liu, X., & Gonzalez Abad, G. (2024). TROPOMI research ozone profile dataset in August 2022 (Version 1) [Dataset]. *Zenodo*. https://doi.org/10.5281/zenodo.13988537

Bak, J., Liu, X., Yang, K., Gonzalez Abad, G., O'Sullivan, E., Chance, K., & Kim, C.-H. (2024). An improved OMI ozone profile research product version 2.0 with collection 4 L1b data and algorithm updates. *Atmospheric Measurement Techniques*, *17*(7), 1891–1911. https://doi.org/10.5194/amt-17-1891-2024

Bak, J., Song, E.-J., Lee, H.-J., Liu, X., Koo, J.-H., Kim, J., et al. (2022). Temporal variability of tropospheric ozone and ozone profiles in the Korean Peninsula during the East Asian summer monsoon: Insights from multiple measurements and reanalysis datasets. *Atmospheric Chemistry and Physics*, *22*(21), 14177–14187. https://doi.org/10.5194/acp-22-14177-2022

Bian, J., Li, D., Bai, Z., Li, Q., Lyu, D., & Zhou, X. (2020). Transport of Asian surface pollutants to the global stratosphere from the Tibetan Plateau region during the Asian summer monsoon. *National Science Review*, *7*(3), 516–533. https://doi.org/10.1093/nsr/nwaa005

Borsdorff, T., Campos, T., Kille, N., Zarzana, K. J., Volkamer, R., & Landgraf, J. (2023). Vertical information of CO from TROPOMI total column measurements in context of the CAMS-IFS data assimilation scheme. *Atmospheric Measurement Techniques*, *16*(11), 3027–3038. https://doi.org/10.5194/amt-16-3027-2023

Borsdorff, T., de Brugh, J., Hu, H., Aben, I., Hasekamp, O., & Landgraf, J. (2018). Measuring carbon monoxide with TROPOMI: First results and a comparison with ECMWF-IFS analysis data. *Geophysical Research Letters*, *45*(6), 2826–2832. https://doi.org/10.1002/2018GL077045

Chen, W., & Chou, C. (2022). ACCLIP: Pengjia Islet Ozonesonde Data (Version 1.0) [Dataset]. *UCAR/NCAR – Earth Observing Laboratory*. https://doi.org/10.26023/GH72-H4H2-RN13

Chiu, R., Obersteiner, F., Franchin, A., Campos, T., Bailey, A., Webster, C., et al. (2024). Intercomparison of fast airborne ozone instruments to measure eddy covariance fluxes: Spatial variability in deposition at the ocean surface and evidence for cloud processing. *Atmospheric Measurement Techniques*, *17*(19), 5731–5746. https://doi.org/10.5194/amt-17-5731-2024

Copernicus Sentinel data processed by ESA, Koninklijk Nederlands Meteorologisch Instituut (KNMI)/Netherlands Institute for Space Research (SRON). (2019). Sentinel-5P TROPOMI Carbon Monoxide (CO) Column 1-Orbit L2, 5.5 km × 7 km (Version 2) [Dataset]. *NASA Goddard Earth Sciences Data and Information Services Center (GES DISC)*. https://doi.org/10.5270/S5P-bj3nry0

Diao, M., Jensen, J. B., Pan, L. L., Homeyer, C. R., Honomichl, S., Bresch, J. F., & Bansemer, A. (2015). Distributions of ice supersaturation and ice crystals from airborne observations in relation to upper tropospheric dynamical boundaries. *Journal of Geophysical Research: Atmospheres*, *120*(10), 5101–5121. https://doi.org/10.1002/2015JD023139

Gao, R. S., Ballard, J., Watts, L. A., Thornberry, T. D., Ciciora, S. J., McLaughlin, R. J., & Fahey, D. W. (2012). A compact, fast UV photometer for measurement of ozone from research aircraft. *Atmospheric Measurement Techniques*, *5*(9), 2201–2210. https://doi.org/10.5194/amt-5-2201-2012

Gelaro, R., McCarty, W., Suárez, M. J., Todling, R., Molod, A., Takacs, L., et al. (2017). The Modern-Era Retrospective Analysis for Research and Applications, Version 2 (MERRA-2). *Journal of Climate*, *30*(13), 5419–5454. https://doi.org/10.1175/JCLI-D-16-0758.1

Gettelman, A., & Sobel, A. H. (2000). Direct diagnoses of stratosphere–troposphere exchange. *Journal of the Atmospheric Sciences*, *57*(1), 3–16. https://doi.org/10.1175/1520-0469(2000)057<0003:DDOSTE>2.0.CO;2

Global Modeling and Assimilation Office (GMAO). (2015). inst3_3d_asm_Cp: MERRA-2 3D IAU State, Meteorology Instantaneous 3-hourly (p-coord, 0.625x0.5L42) (Version 5.12.4) [Dataset]. *NASA Goddard Space Flight Center Distributed Active Archive Center (GSFC DAAC)*. https://doi.org/10.5067/QBZ6MG944HW0

Guan, W., Hu, H., Ren, X., & Yang, X.-Q. (2019). Subseasonal zonal variability of the western Pacific subtropical high in summer: Climate impacts and underlying mechanisms. *Climate Dynamics*, *53*(5), 3325–3344. https://doi.org/10.1007/s00382-019-04705-4

He, Y. J., Uno, I., Wang, Z. F., Pochanart, P., Li, J., & Akimoto, H. (2008). Significant impact of the East Asia monsoon on ozone seasonal behavior in the boundary layer of Eastern China and the west Pacific region. *Atmospheric Chemistry and Physics*, *8*(24), 7543–7555. https://doi.org/10.5194/acp-8-7543-2008

Hoskins, B. J., & Rodwell, M. J. (1995). A model of the Asian summer monsoon, I, the global scale. *Journal of Atmospheric Sciences*, *52*, 1329–1340.

Honomichl, S. (2023). ACCLIP NSF/NCAR GV Instrument Data Merges – 10 Second (Version 1.0) [Dataset]. *UCAR/NCAR – Earth Observing Laboratory*. https://doi.org/10.26023/2HAX-YPQB-GG0Q

Honomichl, S. B., & Pan, L. L. (2020). Transport from the Asian summer monsoon anticyclone over the western Pacific. *Journal of Geophysical Research: Atmospheres*, *125*(13), e2019JD032094. https://doi.org/10.1029/2019JD032094

Jacob, D. J., Logan, J. A., & Murti, P. P. (1999). Effect of rising Asian emissions on surface ozone in the United States. *Geophysical Research Letters*, *26*(14), 2175–2178. https://doi.org/10.1029/1999GL900450

Kim, J., & Koo, J. (2024). ACCLIP: Anmyeon Ozonesonde Data (Version 2.0) [Dataset]. *UCAR/NCAR – Earth Observing Laboratory*. https://doi.org/10.26023/39Y4-9RAB-5A0K

Kurokawa, J., & Ohara, T. (2020). Long-term historical trends in air pollutant emissions in Asia: Regional Emission inventory in ASia (REAS) version 3. *Atmospheric Chemistry and Physics*, *20*(21), 12761–12793. https://doi.org/10.5194/acp-20-12761-2020

Liang, Q., Newman, P. A., Fleming, E. L., Lait, L. R., Atlas, E., Pan, L., et al. (2025). Asian summer monsoon anticyclone—The primary entryway for chlorinated very-short-lived substances to the stratosphere. *Geophysical Research Letters*, *52*(3), e2024GL110248. https://doi.org/10.1029/2024GL110248

Liu, S., Zhao, W., Li, L., Jin, J., Li, T., Xu, H., & Zhao, W. (2023). Meteorological mechanisms of regional $PM_{2.5}$ and O_3 transport in the North China Plain driven by the East Asian monsoon. *Atmospheric Pollution Research*, *14*(1), 101638. https://doi.org/10.1016/j.apr.2022.101638

Livesey, N. J., Filipiak, M. J., Froidevaux, L., Read, W. G., Lambert, A., Santee, M. L., et al. (2008). Validation of Aura Microwave Limb Sounder O_3 and CO observations in the upper troposphere and lower stratosphere. *Journal of Geophysical Research*, *113*(D15), D15S02. https://doi.org/10.1029/2007JD008805

Livesey, N. J., Read, W. G., Wagner, P. A., Froidevaux, L., Santee, M. L., Schwartz, M. J., et al. (2022). *Version 5.0x Level 2 and 3 data quality and description document (MLS)*. Jet Propulsion Laboratory. Retrieved from https://mls.jpl.nasa.gov/data/v5-0_data_quality_document.pdf

Lu, X., Zhang, L., Liu, X., Gao, M., Zhao, Y., & Shao, J. (2018). Lower tropospheric ozone over India and its linkage to the South Asian monsoon. *Atmospheric Chemistry and Physics*, *18*(5), 3101–3118. https://doi.org/10.5194/acp-18-3101-2018

Luo, J., Pan, L. L., Honomichl, S. B., Bergman, J. W., Randel, W. J., Francis, G., et al. (2018). Space-time variability in UTLS chemical distribution in the Asian summer monsoon viewed by limb and nadir satellite sensors. *Atmospheric Chemistry and Physics*, *18*(16), 12511–12530. https://doi.org/10.5194/acp-18-12511-2018

McManus, J. B., Zahniser, M. S., Nelson, D. D., Jr., Shorter, J. H., Herndon, S. C., Wood, E. C., & Wehr, R. (2010). Application of quantum cascade lasers to high-precision atmospheric trace gas measurements. *Optical Engineering*, *49*(11), 111124. https://doi.org/10.1117/1.3498782

NASA. (2025). ACCLIP WB-57 aircraft in-situ trace gas data [Dataset]. *NASA*. https://doi.org/10.5067/SUBORBITAL/ACCLIP/DATA001

Pan, L. L., Atlas, E. L., Honomichl, S. B., Smith, W. P., Kinnison, D. E., Solomon, S., et al. (2024). East Asian summer monsoon delivers large abundances of very short-lived organic chlorine substances to the lower stratosphere. *Proceedings of the National Academy of Sciences*, *121*(12), e2318716121. https://doi.org/10.1073/pnas.2318716121

Pan, L. L., Honomichl, S. B., Kinnison, D. E., Abalos, M., Randel, W. J., Bergman, J. W., & Bian, J. (2016). Transport of chemical tracers from the boundary layer to stratosphere associated with the dynamics of the Asian summer monsoon. *Journal of Geophysical Research: Atmospheres*, *121*(23), 14159–14174. https://doi.org/10.1002/2016JD025616

Pan, L. L., Kinnison, D., Liang, Q., Chin, M., Santee, M. L., Flemming, J., et al. (2022). A multimodel investigation of Asian summer monsoon UTLS transport over the Western Pacific. *Journal of Geophysical Research: Atmospheres*, *127*, e2022JD037511. https://doi.org/10.1029/2022JD037511

Pan, L. L., Paulik, L. C., Honomichl, S. B., Munchak, L. A., Bian, J., Selkirk, H. B., & Vömel, H. (2014). Identification of the tropical tropopause transition layer using the ozone-water vapor relationship. *Journal of Geophysical Research: Atmospheres*, *119*(6), 3586–3599. https://doi.org/10.1002/2013JD020558

Park, M., Randel, W. J., Gettelman, A., Massie, S. T., & Jiang, J. H. (2007). Transport above the Asian summer monsoon anticyclone inferred from Aura Microwave Limb Sounder tracers. *Journal of Geophysical Research*, *112*(16), 1–13. https://doi.org/10.1029/2006JD008294

Park, M., Randel, W. J., Kinnison, D. E., Garcia, R. R., & Choi, W. (2004). Seasonal variation of methane, water vapor, and nitrogen oxides near the tropopause: Satellite observations and model simulations. *Journal of Geophysical Research*, *109*(D3), D03302. https://doi.org/10.1029/2003JD003706

Ramanathan, V., & Feng, Y. (2009). Air pollution, greenhouse gases and climate change: Global and regional perspectives. *Atmospheric Environment*, *43*(1), 37–50. https://doi.org/10.1016/j.atmosenv.2008.09.063

Randel, W. J., Park, M., Emmons, L., Kinnison, D., Bernath, P., Walker, K. A., et al. (2010). Asian monsoon transport of pollution to the stratosphere. *Science*, *328*(5978), 611–613. https://doi.org/10.1126/science.1182274

Ridley, B. A., & Grahek, F. E. (1990). A small, low flow, high sensitivity reaction vessel for NO chemiluminescence detectors. *Journal of Atmospheric and Oceanic Technology*, *7*(2), 307–311. https://doi.org/10.1175/1520-0426(1990)007<0307:ASLFHS>2.0.CO;2

Schwartz, M., Pumphrey, H., Livesey, N., & Read, W. (2020). ML2CO: MLS/Aura Level 2 Carbon Monoxide (CO) Mixing Ratio (Version 005) [Dataset]. *NASA Goddard Earth Sciences Data and Information Services Center (GES DISC)*. https://doi.org/10.5067/Aura/MLS/DATA2506

Shen, L., Jacob, D. J., Liu, X., Huang, G., Li, K., Liao, H., & Wang, T. (2019). An evaluation of the ability of the Ozone Monitoring Instrument (OMI) to observe boundary layer ozone pollution across China: Application to 2005–2017 ozone trends. *Atmospheric Chemistry and Physics*, *19*(9), 6551–6560. https://doi.org/10.5194/acp-19-6551-2019

Shen, L., Liu, J., Zhao, T., Xu, X., Han, H., Wang, H., & Shu, Z. (2022). Atmospheric transport drives regional interactions of ozone pollution in China. *Science of the Total Environment*, *830*, 154634. https://doi.org/10.1016/j.scitotenv.2022.154634

Shin, D., Kim, J., & Park, S. (2023). ACCLIP: Pohang Ozonesonde Data (Version 1.0) [Dataset]. *UCAR/NCAR – Earth Observing Laboratory*. https://doi.org/10.26023/12PY-NA9V-Z903

Smit, H., Straeter, W., Johnson, B. J. J., Oltmans, S. J., Davies, J., Tarasick, D. W., et al. (2007). Assessment of the performance of ECC-ozonesondes under quasi-flight conditions in the environmental simulation chamber: Insights from the Juelich Ozone Sonde Intercomparison Experiment (JOSIE). *Journal of Geophysical Research*, *112*(D19), D19306. https://doi.org/10.1029/2006jd007308

Smit, H. G. J., Poyraz, D., Van Malderen, R., Thompson, A. M., Tarasick, D. W., Stauffer, R. M., et al. (2024). New insights from the Jülich Ozone Sonde Intercomparison Experiment: Calibration functions traceable to one ozone reference instrument. *Atmospheric Measurement Techniques*, *17*(1), 73–112. https://doi.org/10.5194/amt-17-73-2024

Smith, W. P., Pan, L. L., Ueyama, R., Honomichl, S., Campos, T., Viciani, S., et al. (2025). Transport by Asian summer monsoon convection to the upper troposphere and lower stratosphere during ACCLIP (2022). *Journal of Geophysical Research: Atmospheres*, *130*(7), e2024JD042732. https://doi.org/10.1029/2024JD042732

Vadrevu, K., Ohara, T., & Justice, C. (2017). Land cover, land use changes and air pollution in Asia: A synthesis. *Environmental Research Letters*, *12*(12), 120201. https://doi.org/10.1088/1748-9326/aa9c5d

van Aardenne, J. A., Carmichael, G. R., Levy, H., Streets, D., & Hordijk, L. (1999). Anthropogenic NO_x emissions in Asia in the period 1990–2020. *Atmospheric Environment*, *33*(4), 633–646. https://doi.org/10.1016/S1352-2310(98)00110-1

Veefkind, J. P., Aben, I., McMullan, K., Förster, H., de Vries, J., Otter, G., et al. (2012). TROPOMI on the ESA Sentinel-5 Precursor: A GMES mission for global observations of the atmospheric composition for climate, air quality and ozone layer applications. *Remote Sensing of Environment*, *120*, 70–83. https://doi.org/10.1016/j.rse.2011.09.027

Vogel, B., Günther, G., Müller, R., Grooß, J.-U., & Riese, M. (2015). Impact of different Asian source regions on the composition of the Asian monsoon anticyclone and of the extratropical lowermost stratosphere. *Atmospheric Chemistry and Physics*, *15*, 13699–13716. https://doi.org/10.5194/acp-15-13699-2015

Vogel, B., Pan, L. L., Konopka, P., Günther, G., Müller, R., Hall, W., et al. (2011). Transport pathways and signatures of mixing in the extratropical tropopause region derived from Lagrangian model simulations. *Journal of Geophysical Research*, *116*(D5), D05306. https://doi.org/10.1029/2010JD014876

von Hobe, M., Ploeger, F., Konopka, P., Kloss, C., Ulanowski, A., Yushkov, V., et al. (2021). Upward transport into and within the Asian monsoon anticyclone as inferred from StratoClim trace gas observations. *Atmospheric Chemistry and Physics*, *21*(2), 1267–1285. https://doi.org/10.5194/acp-21-1267-2021

Wang, S., & Yuan, X. (2018). Extending seasonal predictability of Yangtze River summer floods. *Hydrology and Earth System Sciences*, *22*(8), 4201–4211. https://doi.org/10.5194/hess-22-4201-2018

Wang, X., Randel, W., Pan, L., Wu, Y., & Zhang, P. (2022). Transient behavior of the Asian summer monsoon anticyclone associated with eastward eddy shedding. *Journal of Geophysical Research: Atmospheres*, *127*(6), e2021JD036090. https://doi.org/10.1029/2021JD036090

Waters, J. W., Froidevaux, L., Harwood, R. S., Jarnot, R. F., Pickett, H. M., Read, W. G., et al. (2006). The Earth observing system microwave limb sounder (EOS MLS) on the aura Satellite. *IEEE Transactions on Geoscience and Remote Sensing*, *44*(5), 1075–1092. https://doi.org/10.1109/TGRS.2006.873771

World Meteorological Organization. (1957). Definition of the tropopause. *Bulletin of the World Meteorological Organization*, *6*, 136–137.

Yates, E. L., Golston, L. M., Podolske, J. R., Iraci, L. T., Okorn, K. E., Dang, C., et al. (2025). Description and validation of a carbon monoxide and nitrous oxide instrument for high-altitude airborne science (COMA). *EGUsphere*, *2025*, 1–17. https://doi.org/10.5194/egusphere-2025-1081

Zhao, N., Manda, A., Guo, X., & Wang, B. (2022). Impacts of moisture supply from the subtropical western Pacific on the subtropical high and the atmospheric river during the heavy rain of 2020 in Japan. *Frontiers in Earth Science*, *10*, 1–14. https://doi.org/10.3389/feart.2022.1043093

Zhou, T., & Li, Z. (2002). Simulation of the East Asian summer monsoon using a variable resolution atmospheric GCM. *Climate Dynamics*, *19*(2), 167–180. https://doi.org/10.1007/s00382-001-0214-8

Zhu, Y., Yu, P., Wang, X., Bardeen, C., Borrmann, S., Höpfner, M., et al. (2024). Evaluating the importance of nitrate-containing aerosols for the Asian tropopause aerosol layer. *Journal of Geophysical Research: Atmospheres*, *129*(19), e2024JD041283. https://doi.org/10.1029/2024JD041283